Received 2 April 2025
Revised 25 April 2025
Accepted 25 April 2025

A digital-twin-based open circuit fault diagnosis method for permanent magnet motor drive system

Leiting Zhao
Department of AC transmission Development, China Academy of Railway Sciences Corporation Limited, Beijing, China
Zheng Ruan
Fundamental Research and Development Department, China Academy of Railway Sciences Corporation Limited, Locomotive and Car Research Institute, Beijing, China
Kan Liu
China Academy of Railway Sciences Corporation Limited, Locomotive and Car Research Institute, Beijing, China
Liran Li
Department of AC transmission Development, China Academy of Railway Sciences Corporation Limited, Beijing, China, and
Yuchao Zou
School of Electrical Engineering, Southwest Jiaotong University, Chengdu, China

Abstract

Purpose – This study aims to implement condition monitoring for urban rail train permanent magnet synchronous motors and inverter systems. Through the construction of a digital twin model, it performs fault diagnosis of potential system failures, enabling rapid fault localization and protection.

Design/methodology/approach – This research begins with a brief introduction to the structure and classification of permanent magnet synchronous motors (PMSMs), followed by a detailed analysis of their mathematical model. Subsequently, it thoroughly investigates the working principle of three-phase two-level inverters and the distribution of space voltage vectors. Based on the analysis of the main circuit topology, a digital twin model matching the external characteristics of the physical circuit is established using the model predictive control method, achieving accurate system simulation. Furthermore, through theoretical analysis and simulation verification of phase current characteristics under inverter switch tube faults, general patterns of phase currents under fault conditions are summarized. The established digital twin model is then employed to validate these patterns, confirming the model's effectiveness in fault diagnosis.

Findings – This study proposes a fault diagnosis method based on digital twins. Experimental and simulation results demonstrate that the established digital twin model can accurately simulate the external characteristics of the actual physical circuit, validating its effectiveness in inverter fault diagnosis. This approach offers practical value for condition monitoring in actual urban rail train systems.

Originality/value – The study innovatively starts from a mathematical model and simulates the actual physical model through a virtual model, requiring only external characteristics to achieve system fault diagnosis, thereby enhancing diagnostic efficiency.

Keywords Urban rail train, Digital twin, Fault diagnosis, IGBT

Paper type Research paper

Funding: This work is supported by the Fund of China State Railway Group Corporation Limited (L2023J001), and the Fund of China Academy of Railway Sciences Corporation Limited (2023YJ247).

Railway Sciences
Vol. 4 No. 4, 2025
pp. 494-521
Emerald Publishing Limited
e-ISSN: 2755-0915
p-ISSN: 2755-0907
DOI 10.1108/RS-04-2025-0008

1. Introduction and literature review

In recent years, urban rail transit has experienced rapid development, with continuous advancements in overcoming related technical challenges. As a primary mode of public transportation in cities (Yang *et al.*, 2011), urban rail transit plays a pivotal role in alleviating traffic congestion and reducing urban transportation pressure. The increasing urbanization and population density in metropolitan areas have necessitated the expansion and modernization of urban rail systems to meet the growing demand for efficient and sustainable transportation solutions. This has led to significant investments in research and development, focusing on enhancing the performance, reliability, and safety of urban rail transit systems.

The traction drive system, a critical component for the reliable operation of rail vehicles, primarily consists of the pantograph, intermediate DC link, traction inverter, and traction motor (Lin, Fang, Wang, Yang, & Lin, 2021), as illustrated in Figure 1. Among these, the motor traction system (comprising the traction inverter and traction motor) serves as the core of the traction drive system (Choo & Won, 2020). Its performance directly influences key operational aspects of the train, such as starting, braking, and speed control. Consequently, enhancing its reliability is essential for ensuring the safe operation of urban rail vehicles. The traction drive system must operate under varying load conditions, environmental factors, and operational stresses, making it susceptible to wear and tear over time. Therefore, continuous monitoring and maintenance of this system are crucial to prevent unexpected failures and ensure uninterrupted service.

Permanent Magnet Synchronous Motors (PMSMs) have gained significant traction due to their high power density, superior efficiency, and exceptional performance. The permanent magnet synchronous traction system for urban rail transit refers to the traction system utilizing PMSMs in urban rail vehicles. Currently, an increasing number of urban rail transit systems globally are adopting permanent magnet traction motors (Hammoud *et al.*, 2022; Faiz & Mazaheri-Tehrani, 2016). As a result, monitoring the parameter states of PMSMs is crucial for maintaining the reliable operation of urban rail transit vehicles. PMSMs offer several advantages over traditional induction motors, including higher efficiency, better power factor, and reduced maintenance requirements. These benefits make PMSMs an attractive choice for modern urban rail systems, where energy efficiency and operational reliability are paramount.

As equipment service life extends (Liu, Zhu, & Stone, 2013), component wear and aging progressively worsen, prompting significant research interest in fault diagnosis technologies for power devices. Various fault diagnosis methods have been continuously proposed. Fault diagnosis primarily involves detecting faults, identifying their locations, and implementing fault-tolerant control or isolation measures to ensure system safety. Among these, diagnostic methods for open-circuit faults caused by inverter IGBT failures can be broadly classified into three categories: signal processing-based methods (Da, Shi, & Krishnamurthy, 2012), analytical model-based methods (Underwood & Husain, 2009), and data-driven methods (Wang, Zhang, Wang, & Xu, 2019). Each of these methods has its unique advantages and limitations, and the choice of method often depends on the specific application and operational requirements.

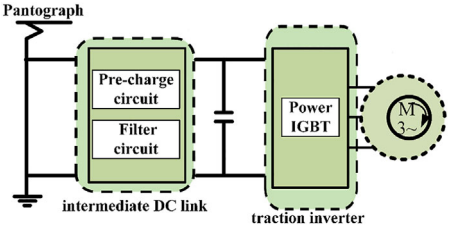

Figure 1. Electric traction drive system for urban rail transit trains. Source: Authors' own work

Signal processing-based diagnostic methods for inverter open-circuit faults primarily rely on the electrical signals of the inverter (Odhano, Bojoi, Roşu, & Tenconi, 2015). By employing advanced signal processing techniques, these methods analyze distortions in voltage and current signals caused by IGBT failures, extracting diagnostic variables such as phase, amplitude, and average values. The state of these variables is then analyzed to achieve fault diagnosis and localization. Voltage-based methods offer the fastest diagnostic speed and highest accuracy (Wu, Fu, Lin, & Jia, 2019); however, they often require additional voltage sensors, increasing system complexity and cost. Current-based diagnostic methods, while more cost-effective, typically require longer diagnostic times to ensure higher accuracy. The choice between voltage and current-based methods often involves a trade-off between diagnostic speed, accuracy, and system complexity.

Analytical model-based methods involve constructing physical and mathematical mechanistic models (Liu, Zhang, Chen, Zhu, & Zhang, 2010; Shi, Sun, Huang, & Li, 2011). State variables derived from these models are compared with actual measurements to generate residuals. Fault diagnosis is achieved by analyzing and comparing these residuals across different fault types. These methods are particularly useful for understanding the underlying mechanisms of faults and developing robust diagnostic algorithms. However, they often require detailed knowledge of the system's physical and mathematical properties, which can be challenging to obtain in complex systems.

Data-driven open-circuit fault diagnosis methods primarily leverage artificial intelligence algorithms for offline data training, creating a fault-type network that correlates fault signals with specific fault types (Zhang, Liu, Wan, & Feng, 2021). Common artificial intelligence algorithms include neural networks, support vector machines, fuzzy logic, and principal component analysis, among others. These methods are particularly effective in handling large volumes of data and identifying complex patterns that may not be easily detectable using traditional methods. However, they often require significant computational resources and extensive training data to achieve high accuracy.

The concept of the digital twin first emerged in 2003 (Grieves, 2005), initially termed the "Mirror Space Model," and was introduced by Professor Grieves M.W. at the University of Michigan in the Product Lifecycle Management (PLM) curriculum. The digital twin concept was first applied in the aerospace and defense sectors. In 2010, the National Aeronautics and Space Administration (NASA) pioneered the use of "digital twin" technology to create a digital twin of a physical aircraft for design and maintenance purposes (Glaessgen & Stargel, 2012), ensuring its safe operation throughout its lifecycle. This innovative approach has since been adopted across various industries, demonstrating its potential for enhancing system reliability and performance. Digital twins enable real-time monitoring, predictive maintenance, and optimized performance by creating a virtual replica of physical assets. This allows for the simulation of various operational scenarios, identification of potential issues, and implementation of corrective measures before they impact the actual system.

The application of digital twins in urban rail transit systems offers numerous benefits, including improved fault diagnosis, enhanced operational efficiency, and reduced maintenance costs. By creating a digital twin of the traction drive system, operators can monitor the system's performance in real time, predict potential failures, and implement preventive measures to ensure uninterrupted service. This approach not only enhances the reliability and safety of urban rail transit systems but also contributes to the overall sustainability and efficiency of urban transportation networks.

In conclusion, the rapid development of urban rail transit systems has necessitated the adoption of advanced technologies for fault diagnosis and condition monitoring. The integration of digital twins, signal processing, analytical models, and data-driven methods offers a comprehensive approach to enhancing the reliability and performance of traction drive systems. As urban rail transit systems continue to evolve, the adoption of these advanced diagnostic methods will play a crucial role in ensuring their safe and efficient operation.

This paper proposes a digital twin-based open-circuit fault diagnosis method. By establishing a digital twin model of the permanent magnet synchronous motor and its drive system, the characteristic currents of the actual system are compared with those of the digital twin model to identify and locate faulty switching devices, thereby achieving rapid and intelligent fault diagnosis. This method is non-intrusive, requiring no additional monitoring circuits, and does not interfere with the normal operation of the original system.

2. PMSM drive system mathematical model and control strategy

2.1 PMSM drive system mathematical model

The PMSM features a straightforward construction, primarily comprising a stator, rotor, and permanent magnet. Based on the position of the permanent magnet, it can be broadly categorized into: Surface Permanent Magnet Synchronous Motor (SPMSM) and Interior Permanent Magnet Synchronous Motor (IPMSM). Figure 2. depicts the simplified structures of both motor types, respectively.

To obtain a simplified mathematical model of the PMSM, the following reasonable assumptions are typically made:

(1) core saturation is not considered.

(2) eddy current and hysteresis losses are neglected.

(3) three-phase currents are symmetric sinusoidal.

(4) the motor parameters remain almost constant regardless of operating conditions.

After satisfying these conditions, an accurate mathematical model in the three-phase stationary coordinate system of the PMSM can be derived as

$$\begin{bmatrix} u_A \\ u_B \\ u_C \end{bmatrix} = \begin{bmatrix} R_s & 0 & 0 \\ 0 & R_s & 0 \\ 0 & 0 & R_s \end{bmatrix} \begin{bmatrix} i_A \\ i_B \\ i_C \end{bmatrix} + \frac{d}{dt} \begin{bmatrix} \psi_A \\ \psi_B \\ \psi_C \end{bmatrix} \tag{1}$$

The stator flux linkage equation:

$$\begin{bmatrix} \psi_A \\ \psi_B \\ \psi_C \end{bmatrix} = \begin{bmatrix} L_{AA} & M_{AB} & M_{AC} \\ M_{BA} & L_{BB} & M_{BC} \\ M_{CA} & M_{CB} & L_{CC} \end{bmatrix} \begin{bmatrix} i_A \\ i_B \\ i_C \end{bmatrix} + \begin{bmatrix} \cos\theta \\ \cos(\theta - 2\pi/3) \\ \cos(\theta + 2\pi/3) \end{bmatrix} \psi_f \tag{2}$$

Additionally, through the theory of coordinate transformation, the three-phase stationary coordinate system is transformed into the α-β coordinate system and the d-q coordinate system, and then mathematical models in the α-β and d-q coordinate systems are established.

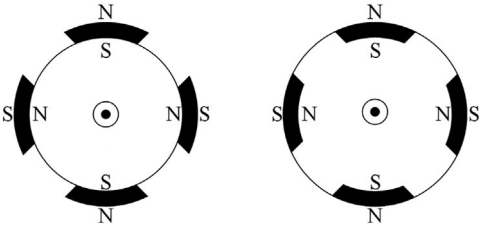

Figure 2. PMSM structure and classification. Source: Authors' own work

Clark transformation:

$$C_{3s/2s} = \frac{2}{3}\begin{bmatrix} 1 & -\frac{1}{2} & -\frac{1}{2} \\ 0 & \frac{\sqrt{3}}{2} & -\frac{\sqrt{3}}{2} \end{bmatrix} \tag{3}$$

Park transformation:

$$C_{2s/2r} = \begin{bmatrix} \cos\theta & \sin\theta \\ -\sin\theta & \cos\theta \end{bmatrix} \tag{4}$$

According to the Equation (3) and (4), the mathematical model of the PMSM can be transformed into α-β and d-q coordinate systems.

$$\begin{bmatrix} u_\alpha \\ u_\beta \end{bmatrix} = \begin{bmatrix} R_s & 0 \\ 0 & R_s \end{bmatrix}\begin{bmatrix} i_\alpha \\ i_\beta \end{bmatrix} + \frac{d}{dt}\begin{bmatrix} \psi_\alpha \\ \psi_\beta \end{bmatrix} \tag{5}$$

The stator flux linkage equation:

$$\begin{bmatrix} \psi_\alpha \\ \psi_\beta \end{bmatrix} = \boldsymbol{L}_{\alpha\beta}\begin{bmatrix} i_\alpha \\ i_\beta \end{bmatrix} + \begin{bmatrix} \cos\theta \\ \sin\theta \end{bmatrix}\psi_f \tag{6}$$

Where $L_{\alpha\beta}$ is the inductance matrix, which can be expressed as:

$$L_{\alpha\beta} = \begin{bmatrix} L_0 + L_1\cos(2\theta) & L_1\sin(2\theta) \\ L_1\sin(2\theta) & L_0 - L_1\cos(2\theta) \end{bmatrix} \tag{7}$$

L_0 and L_1 can be represented by the direct-axis and quadrature-axis inductances of the PMSM as:

$$L_0 = \frac{L_d + L_q}{2}, L_1 = \frac{L_d - L_q}{2} \tag{8}$$

The electromagnetic torque equation is as follows:

$$T_e = \frac{3}{2}n_p(\psi_\alpha i_\alpha - \psi_\beta i_\beta) \tag{9}$$

The differential equation in the d-q coordinate system can be expressed as

$$\begin{bmatrix} u_d \\ u_q \end{bmatrix} = \begin{bmatrix} R_s & 0 \\ 0 & R_s \end{bmatrix}\begin{bmatrix} i_d \\ i_q \end{bmatrix} + \begin{bmatrix} L_d & 0 \\ 0 & L_q \end{bmatrix}\frac{d}{dt}\begin{bmatrix} i_d \\ i_q \end{bmatrix} + \begin{bmatrix} -L_q i_q \\ L_d i_d \psi_f \end{bmatrix}\omega_e \tag{10}$$

The electromagnetic torque equation is as follows:

$$T_e = \frac{3}{2}n_p\left[\psi_f i_q + (L_d - L_q)i_d i_q\right] \tag{11}$$

The topology of the three-phase two-level inverter drive is shown in Figure 3. T_1~T_6 are power switches, and U_{dc} is the DC-side voltage. For subsequent explanation and analysis, the

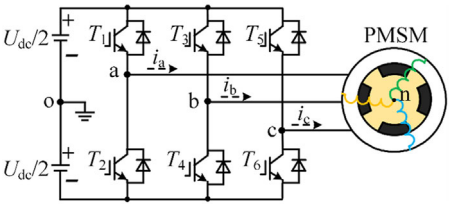

Figure 3. Three-phase two-level inverter topology diagram. Source: Authors' own work

equivalent diagram of the three-phase two-level inverter is shown in Figure 4., with the switching function defined as follows:

$$S_x = \begin{cases} 1 \\ 0 \end{cases}, x = a、\ b、\ c \tag{12}$$

Through analysis, the phase voltages corresponding to different switching states can be obtained in Table 1:

Define the space voltage vector:

$$V_s = \frac{2}{3}\left(u_{an} + u_{bn}e^{j\frac{2\pi}{3}} + u_{cn}e^{j\frac{4\pi}{3}}\right) \tag{13}$$

Therefore, the space voltage vector distribution diagram can be drawn in Figure 5:

Digital twin model: A digital twin is essentially a virtual digital replica of an actual physical system, which can simulate system behaviors and can be used for monitoring, predicting, and

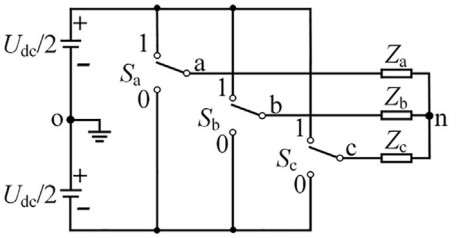

Figure 4. Three-phase two-level inverter equivalent diagram. Source: Authors' own work

Table 1. Inverter switching states and corresponding phase voltages

S_a	S_b	S_c	u_{an}	u_{bn}	u_{cn}
1	1	1	0	0	0
1	1	0	$U_{dc}/3$	$U_{dc}/3$	$-2U_{dc}/3$
1	0	1	$U_{dc}/3$	$-2U_{dc}/3$	$U_{dc}/3$
1	0	0	$2U_{dc}/3$	$-U_{dc}/3$	$-U_{dc}/3$
0	1	1	$-2U_{dc}/3$	$U_{dc}/3$	$U_{dc}/3$
0	1	0	$-U_{dc}/3$	$2U_{dc}/3$	$-U_{dc}/3$
0	0	1	$-U_{dc}/3$	$-U_{dc}/3$	$2U_{dc}/3$
0	0	0	0	0	0

Source(s): Authors' own work

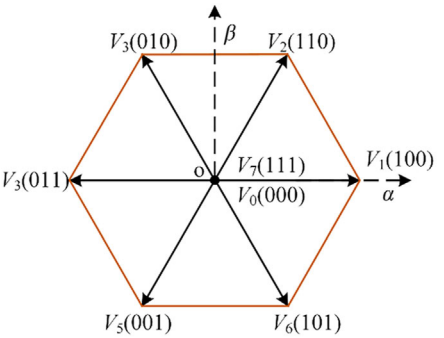

Figure 5. Space voltage vector distribution diagram. Source: Authors' own work

optimizing the system's operating state, performance, and health status. So, in order to obtain the operating state of the three-phase PMSM system, the digital twin modeling of the main circuit and control circuit was carried out. Finally, the digital twin model of the entire closed-loop system was formed.

Main circuit: According to Figures 3 and 4, the output phase voltage of the three-phase inverter can be expressed as:

$$\begin{cases} \mathrm{u}_{\mathrm{an}} = \dfrac{2}{3}\left(S_1\dfrac{U_{\mathrm{dc}}}{2} - S_2\dfrac{U_{\mathrm{dc}}}{2}\right) - \dfrac{1}{3}\left(S_3\dfrac{U_{\mathrm{dc}}}{2} - S_4\dfrac{U_{\mathrm{dc}}}{2}\right) - \dfrac{1}{3}\left(S_5\dfrac{U_{\mathrm{dc}}}{2} - S_6\dfrac{U_{\mathrm{dc}}}{2}\right) \\ u_{\mathrm{bn}} = -\dfrac{1}{3}\left(S_1\dfrac{U_{\mathrm{dc}}}{2} - S_2\dfrac{U_{\mathrm{dc}}}{2}\right) + \dfrac{2}{3}\left(S_3\dfrac{U_{\mathrm{dc}}}{2} - S_4\dfrac{U_{\mathrm{dc}}}{2}\right) - \dfrac{1}{3}\left(S_5\dfrac{U_{\mathrm{dc}}}{2} - S_6\dfrac{U_{\mathrm{dc}}}{2}\right) \\ u_{\mathrm{cn}} = -\dfrac{1}{3}\left(S_1\dfrac{U_{\mathrm{dc}}}{2} - S_2\dfrac{U_{\mathrm{dc}}}{2}\right) - \dfrac{1}{3}\left(S_3\dfrac{U_{\mathrm{dc}}}{2} - S_4\dfrac{U_{\mathrm{dc}}}{2}\right) + \dfrac{2}{3}\left(S_5\dfrac{U_{\mathrm{dc}}}{2} - S_6\dfrac{U_{\mathrm{dc}}}{2}\right) \end{cases} \tag{14}$$

Where S_{i} represents the switching signal (S_{i} is 0 or 1; 1 means conducting, 0 means turned off; $i = 1, 2, 3, 4, 5, 6$); two switches on the same bridge arm cannot be conducting simultaneously.

PMSM modeling primarily utilizes voltage Equation (10). Rewrite the Equation (10) as a current equation:

$$\begin{cases} \dfrac{\mathrm{d}i_{\mathrm{d}}}{dt} = \dfrac{1}{L_{\mathrm{d}}}u_{\mathrm{d}} - \dfrac{R_{\mathrm{s}}}{L_{\mathrm{d}}}i_{\mathrm{d}} + \omega_{\mathrm{e}}\dfrac{L_{\mathrm{q}}}{L_{\mathrm{d}}}i_{\mathrm{q}} \\ \dfrac{di_{\mathrm{q}}}{dt} = \dfrac{1}{L_{\mathrm{q}}}u_{\mathrm{q}} - \dfrac{R_{\mathrm{s}}}{L_{\mathrm{q}}}i_{\mathrm{q}} - \omega_{\mathrm{e}}\dfrac{L_{\mathrm{d}}}{L_{\mathrm{q}}}i_{\mathrm{d}} - \omega_{\mathrm{e}}\dfrac{1}{L_{\mathrm{q}}}\psi_{\mathrm{f}} \end{cases} \tag{15}$$

This paper uses the fourth-order Runge-Kutta method to solve the differential equation. We can obtain the discretized result of the current as:

$$\begin{cases} \mathrm{i}_{\mathrm{dn+1}} = i_{\mathrm{dn}} + \dfrac{h}{6}(K_{\mathrm{a1}} + 2K_{\mathrm{a2}} + 2K_{\mathrm{a3}} + K_{\mathrm{a4}}) \\ i_{\mathrm{qn+1}} = i_{\mathrm{qn}} + \dfrac{h}{6}(K_{\mathrm{b1}} + 2K_{\mathrm{b2}} + 2K_{\mathrm{b3}} + K_{\mathrm{b4}}) \end{cases} \tag{16}$$

Where $i_{\mathrm{dn+1}}$ and $i_{\mathrm{qn+1}}$ are the d-q axis currents at time (n+1); $i_{\mathrm{d,n}}$ and $i_{\mathrm{q,n}}$ are the d-q axis currents at time (n); h is the calculation step size from time (n) to time (n+1); K_{a1}-K_{a4} and K_{b1}-K_{b4} are coefficients, which can be expressed as:

$$
\begin{aligned}
\mathrm{K}_{a1} &= f_1\left(i_{dn}, i_{qn}\right) \\
K_{b1} &= f_2\left(i_{dn}, i_{qn}\right) \\
K_{a2} &= f_1\left(i_{dn}+\frac{h}{2}K_{a1}, i_{qn}+\frac{h}{2}K_{b1}\right) \\
K_{b2} &= f_2\left(i_{dn}+\frac{h}{2}K_{a1}, i_{qn}+\frac{h}{2}K_{b1}\right) \\
K_{a3} &= f_1\left(i_{dn}+\frac{h}{2}K_{a2}, i_{qn}+\frac{h}{2}K_{b2}\right) \\
K_{b3} &= f_2\left(i_{dn}+\frac{h}{2}K_{a2}, i_{qn}+\frac{h}{2}K_{b2}\right) \\
K_{a4} &= f_1\left(i_{dn}+hK_{a3}, i_{qn}+hK_{b3}\right) \\
K_{b4} &= f_2\left(i_{dn}+hK_{a3}, i_{qn}+hK_{b3}\right)
\end{aligned}
\tag{17}
$$

Therefore, using the d-q axis currents (i_{dn}, i_{qn}) and the rotor electrical angular speed (ω_{en}) at time (n), the d-q axis currents (i_{dn+1}, i_{qn+1}) at time (n+1) are obtained. Finally, through coordinate transformation, the ABC three-phase currents are obtained.

2.2 Control circuit:

To obtain an independent twin model, it is also necessary to model the control system. Generally speaking, for a three-phase PMSM control system, the inputs are three-phase currents and the rotor position angle (speed), and the output is the switching signal. This paper adopts Model Predictive Current Control (MPCC) for PMSM control, which is simple to implement and has good dynamic performance. Its control block diagram is shown in Figure 6.

The specific implementation process is as follows:

(1) Three-phase current i_{abc} and rotor position angle θ are sampled.

(2) i_{abc} is transformed to the d-q coordinate system through coordinate transformation to obtain i_{dq}.

(3) delay compensation is applied to i_{dq}.

(4) the current prediction values are obtained using the prediction model.

(5) the control signal is derived by using the i_{dq} prediction values and reference values through the cost function.

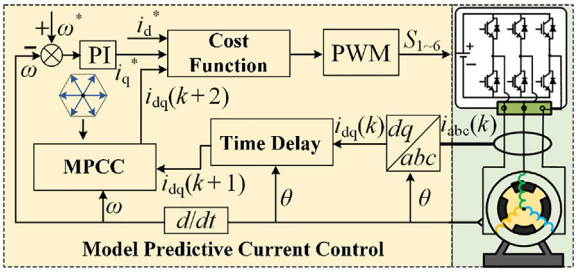

Figure 6. Model predictive current control block diagram. Source: Authors' own work

3. IGBT open-circuit fault diagnosis based on digital twin model

A digital twin model of the three-phase permanent magnet synchronous motor drive system has been established, and the actual parameters of the permanent magnet synchronous motor have been obtained. However, in addition to needing to acquire the operating state of the permanent magnet synchronous motor, the inverter also needs to be monitored. The power device IGBT is the most failure-prone component of the inverter, often leading to inverter open-circuit failures. To minimize the adverse effects of IGBT failures on the system, fault diagnosis should be performed promptly.

3.1 Analysis of IGBT open-circuit fault characteristics:

Due to the low probability of three-tube failures, this paper mainly focuses on single-tube and double-tube fault research. According to the structure of a three-phase two-level inverter, IGBT faults can be classified into 21 types, including 6 types of single-tube faults and 15 types of double-tube faults. The specific fault combinations are shown in Table 2.

3.1.1 IGBT single tube fault. Figure 7 shows the conduction state of the inverter switch and the phase current when a T_1 fault occurs. According to Figure 7(c), when $S_1 = 0$, and $S_2 = 1$, the conduction state of the inverter switch remains the same as when there is no fault, even if a T_1 fault occurs. From Figure 7(a) and Figure 7(b), it can be seen that due to an open-circuit fault in T_1, when $S_1 = 1$, $S_2 = 0$, the current can only flow through the freewheeling diodes D_1 and D_2, causing a change in the circuit topology. This results in the phase voltage and phase current being inconsistent with those of the fault-free condition.

3.1.2 IGBT double tubes fault.

(1) IGBT fault with double tubes on the same side and the same phase

According to Figure 8, when T_1 and T_2 fail, regardless of the values of S_1 and S_2, the current can only flow through the freewheeling diodes D_1 and D_2. Whether it flows through D_1 or D_2

Table 2. Three-phase two-level inverter IGBT fault combinations

Fault type	Fault IGBT
Single tube fault	T_1, T_2, T_3, T_4, T_5, T_6
Co-phase double tube fault	T_1 T_2, T_3 T_4, T_5 T_6
Fault in the double tubes of the same side and different phases	T_1 T_3, T_1 T_5, T_3 T_5, T_2 T_4, T_2 T_6, T_4 T_6
Fault in the double tubes of different sides and different phases	T_1 T_4, T_1 T_6, T_3 T_2, T_3 T_6, T_5 T_2, T_5 T_4

Source(s): Authors' own work

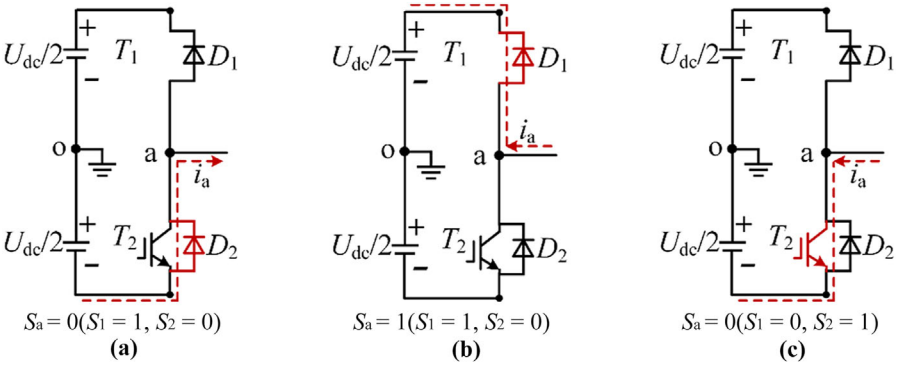

Figure 7. The single-phase switch conduction state of the inverter when T1 fault. Source: Authors' own work

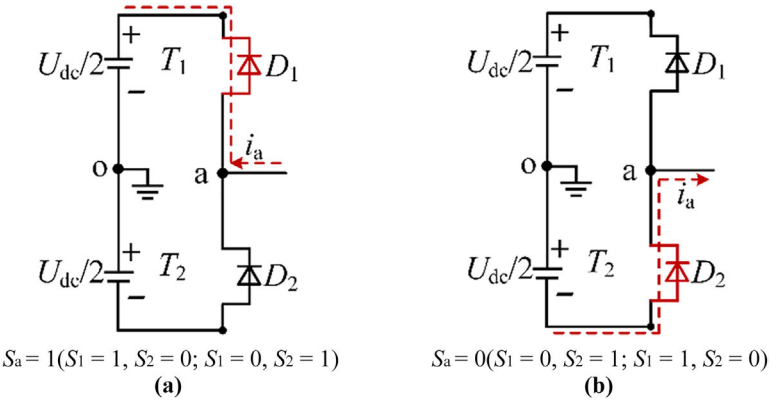

Figure 8. Switch conduction state when double tubes fault on the same side and phase. Source: Authors' own work

depends on the direction of i_a. At this point, the circuit topology changes, resulting in the phase voltage and phase current being inconsistent with those when there is no fault.

(2) IGBT fault with double tubes on the different phases and sides

Taking T_1 and T_4 as an example, Figure 9 shows the conduction state of the inverter switch and the phase current during the open-circuit fault of T_1 and T_4.

(3) IGBT fault with double tubes on the different phases and same sides.

Taking T_1 and T_3 as an example, Figure 10 shows the conduction state of the inverter switch and the phase current during the open-circuit fault of T_1 and T_3.

3.2 IGBT fault diagnosis method

The fault diagnosis process comprises two sequential stages: fault detection and fault localization. As previously analyzed, under normal operating conditions, the output of the actual physical circuit exhibits consistency with the digital twin model, resulting in a negligible difference approaching zero. Conversely, in the event of a fault occurrence, a discernible discrepancy emerges between the outputs of the actual physical circuit and the digital twin model, manifesting as a non-zero difference. Consequently, fault detection can be achieved through comparative analysis of the phase currents between the actual physical circuit and the digital twin model. A fault is considered non-existent when the differential value remains below a predefined threshold; otherwise, a fault condition is confirmed. The schematic representation of this fault diagnosis methodology is illustrated in Figure 11.

Following the confirmation of a fault condition, the subsequent step involves precise localization of the faulty IGBT. The occurrence of a fault induces characteristic distortions in the phase current waveform, which can be systematically identified through comparative analysis of the phase current differentials between the digital twin model and the actual physical circuit during both positive and negative half-cycles. This analytical approach enables accurate fault localization through the identification of specific current distortion patterns associated with IGBT malfunctions.

3.2.1 Model validation.

(1) Steady-state verification:

Figures 12–15 present a comprehensive comparative analysis of the three-phase current waveforms between the digital twin model outputs and the actual physical system

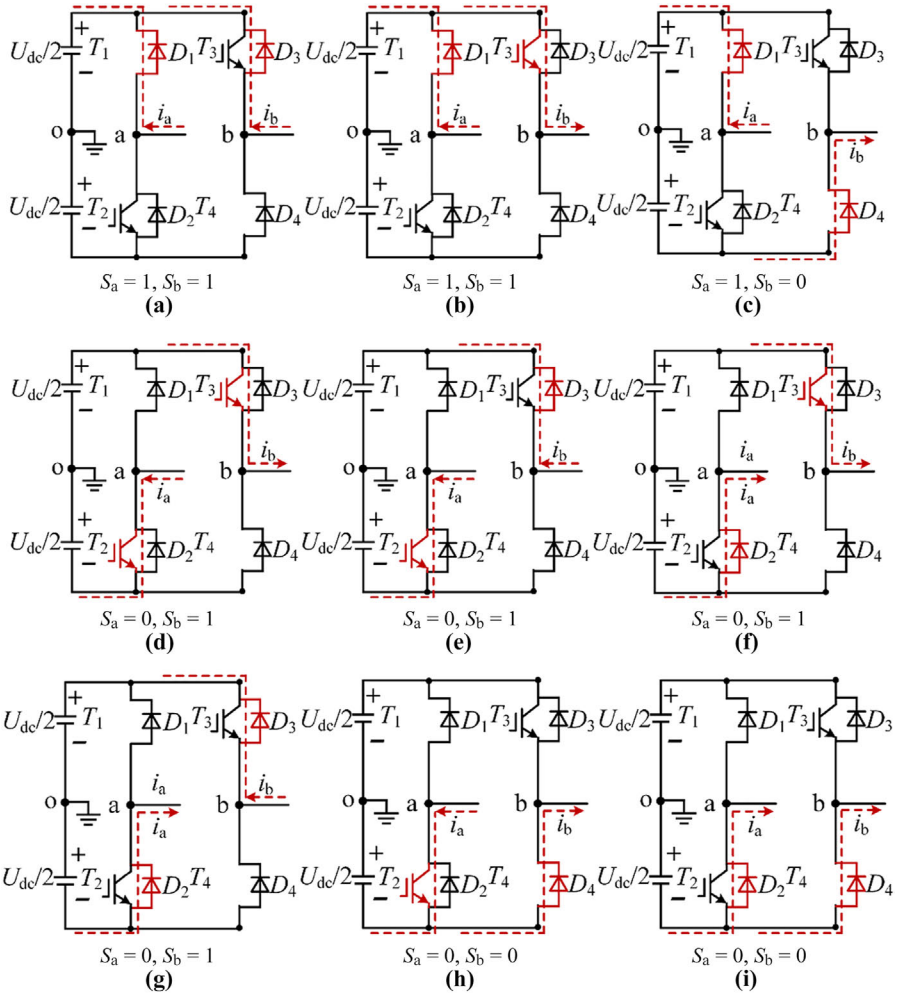

Figure 9. The conduction state of the inverter AB phase switch when T_1, T_4 faults. Source: Authors' own work

measurements under steady-state operating conditions. The waveform comparison, illustrated within a 40ms time window from 2s to 2.04s, demonstrates the model's accuracy. As evidenced in Figures 12 and 13, the digital twin model maintains precise consistency with the actual physical circuit outputs across varying load conditions at constant speed, as indicated by the identical phase current waveforms between the digital twin simulation (digital twin) and physical measurements (physical data). This correspondence confirms the digital twin model's capability to replicate the external characteristics of the physical prototype with high fidelity. Furthermore, the comparative analysis in Figures 13–15 reveals that the digital twin model accurately tracks the physical system behavior under different speed conditions while maintaining a constant load. The phase current outputs from both the digital twin simulation and physical measurements exhibit remarkable consistency, reinforcing the model's robustness in capturing the system's external characteristics across various operational scenarios. These experimental validations collectively demonstrate that the digital twin model of the three-phase permanent magnet synchronous motor drive system achieves sufficient

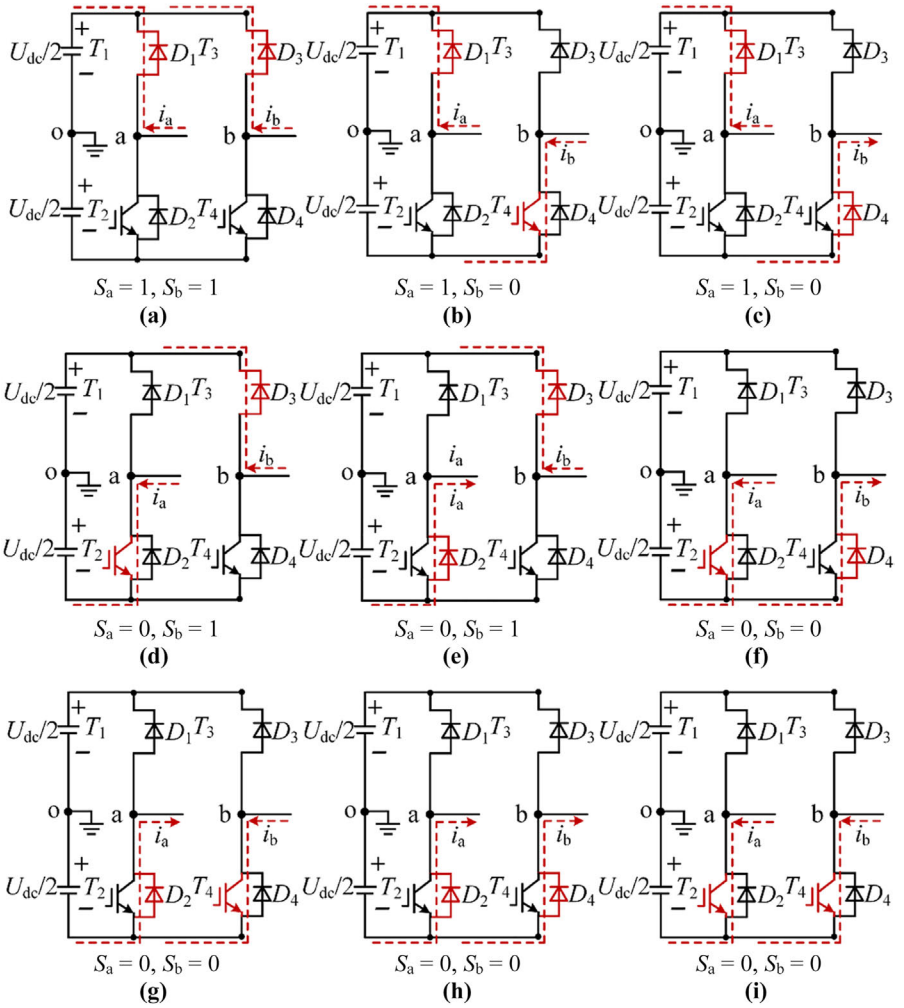

Figure 10. The conduction state of the inverter AB phase switch when T_1, T_3 faults. Source: Authors' own work

accuracy in representing the external characteristics under steady-state conditions, establishing its reliability for subsequent fault diagnosis applications.

(2) Dynamic-state verification:

Figures 16–19 present a comparative analysis of the three-phase current waveforms between the digital twin model outputs and the actual physical system measurements under dynamic operating conditions. The analysis focuses on a 40ms transient period (2s to 2.04s) following simultaneous changes in speed and load torque at $t = 2$s. As demonstrated in Figures 16 and 17, the digital twin model maintains precise waveform correspondence with the physical system measurements during speed variations under constant load conditions. The phase current outputs from both the digital twin simulation (digital twin) and physical measurements (physical data) exhibit identical characteristics, confirming the model's capability to accurately replicate the physical prototype's dynamic response to speed changes.

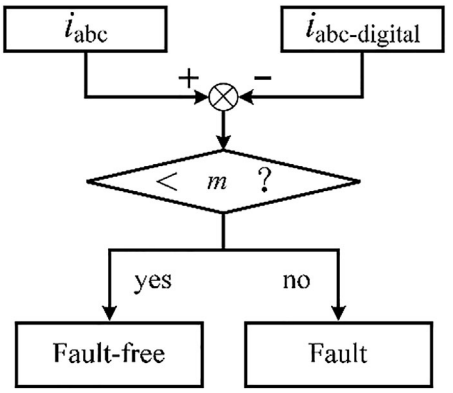

Figure 11. Fault diagnosis flowchart. Source: Authors' own work

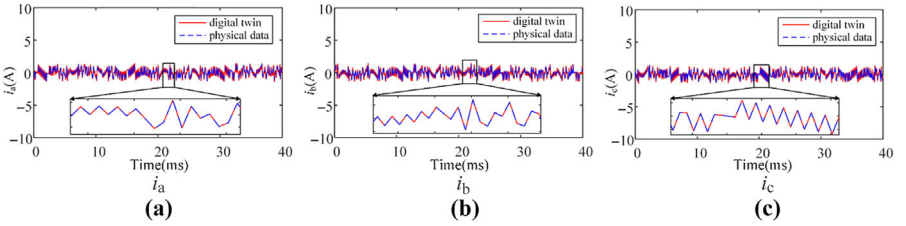

Figure 12. Comparison chart of digital twin and actual three-phase current waveforms (Motor speed = 500r/min,TL = 1N·m). Source: Authors' own work

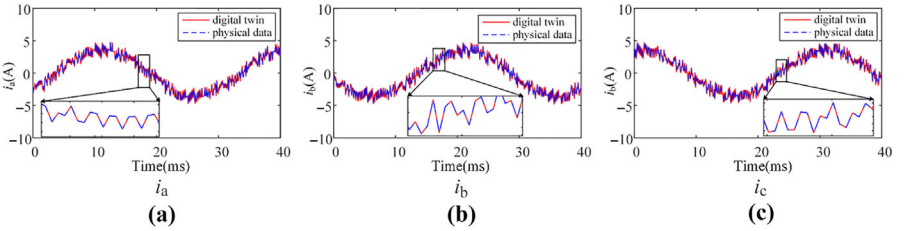

Figure 13. Comparison chart of digital twin and actual three-phase current waveforms (Motor speed = 500r/min, TL = 9N·m). Source: Authors' own work

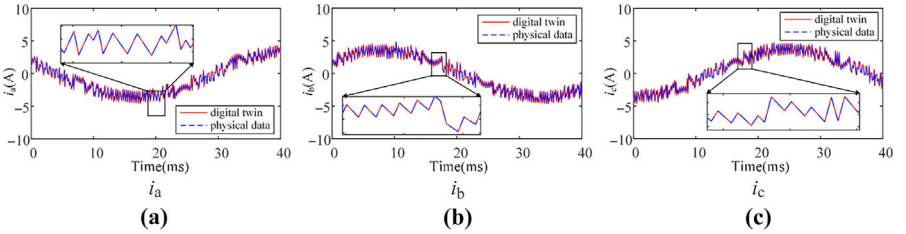

Figure 14. Comparison chart of digital twin and actual three-phase current waveforms (Motor speed = 300r/min, TL = 9N·m). Source: Authors' own work

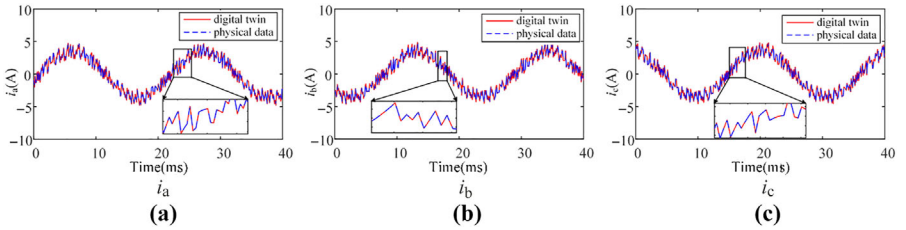

Figure 15. Comparison chart of digital twin and actual three-phase current waveforms (Motor speed = 700r/min, TL = 9N·m). Source: Authors' own work

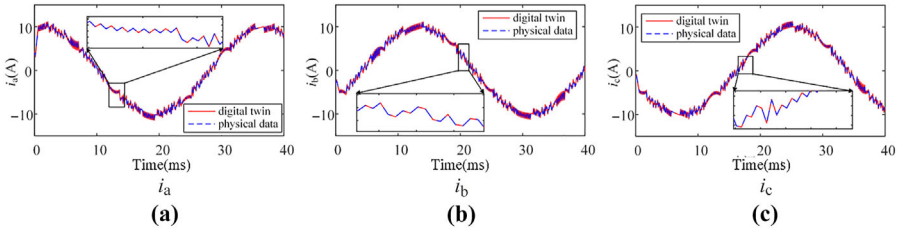

Figure 16. Comparison chart of digital twin and actual three-phase current waveforms (Motor speed = 400r/min~500r/min,TL = 9N·m). Source: Authors' own work

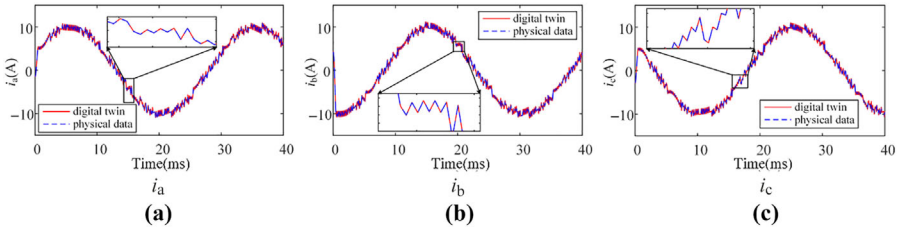

Figure 17. Comparison chart of digital twin and actual three-phase current waveforms (Motor speed = 500r/min~400r/min, TL = 9N·m). Source: Authors' own work

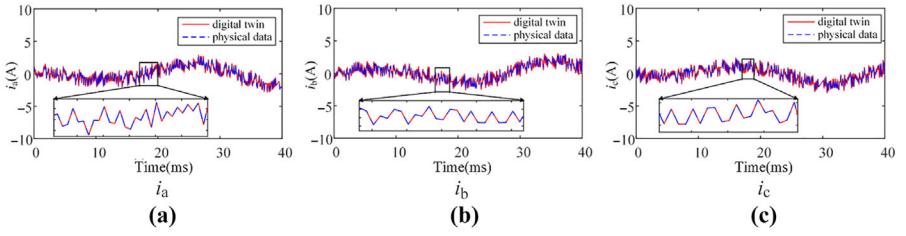

Figure 18. Comparison chart of digital twin and actual three-phase current waveforms (Motor speed = 500r/min, TL = 1N·m~9N·m). Source: Authors' own work

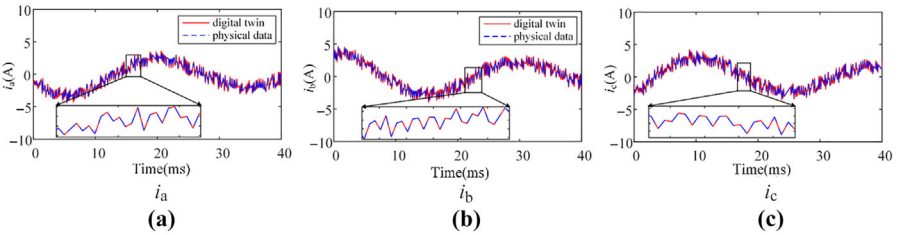

Figure 19. Comparison chart of digital twin and actual three-phase current waveforms (Motor speed = 500r/min, TL = 9N·m∼1N·m). Source: Authors' own work

Furthermore, the experimental results presented in Figures 18 and 19 reveal that the digital twin model effectively tracks the physical system's behavior during load torque variations at a constant speed. The current waveforms from both simulation and measurement show complete consistency, demonstrating the model's robustness in capturing the system's external characteristics under varying load conditions. These comprehensive experimental validations collectively demonstrate that the digital twin model of the three-phase permanent magnet synchronous motor drive system maintains sufficient accuracy in representing the external characteristics under dynamic operating conditions, thereby validating its effectiveness for transient analysis and fault diagnosis applications.

3.2.2 Fault verification analysis:.

(1) single tube fault:

Taking the T_1 fault as an example, Figure 20 shows the $i_{abc\text{-}digital}$ and $i_{abc\text{-}error}$ during the T_1 fault. Table 3 presents the $i_{abc\text{-}digital+}$ and $i_{abc\text{-}digital-}$ during single tube open-circuit fault; Table 4 shows the $i_{abc\text{-}error+}$ and $i_{abc\text{-}error-}$ during single tube open-circuit fault. According to Tables 3 and 4, when T_1 fault, $i_{a\text{-}digital+}$ is almost equal to $i_{a\text{-}error+}$, while the others show significant deviations; when T_2 fault, $i_{a\text{-}digital-}$ is almost equal to $i_{a\text{-}error-}$, and the rest have significant deviations; the fault patterns for T_3, T_4, T_5, and T_6 are the same as those for the single tube failures T_1 and T_2. Therefore, single-tube faults can be accurately diagnosed.

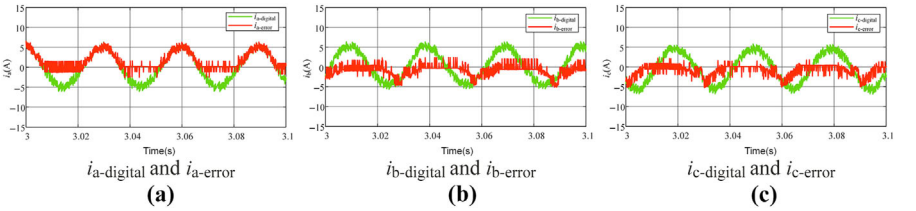

Figure 20. $i_{abc\text{-}digital}$ and $i_{abc\text{-}error}$ when T_1 is fault. Source: Authors' own work

Table 3. $i_{abc\text{-}digital+}$和$i_{abc\text{-}digital-}$ when a single tube fault

Fault type	$i_{a\text{-}digital+}$	$i_{a\text{-}digital-}$	$i_{b\text{-}digital+}$	$i_{b\text{-}digital-}$	$i_{c\text{-}digital+}$	$i_{c\text{-}digital-}$
T_1	3.148	−3.351	3.637	−3.090	3.103	−3.363
T_2	3.150	−3.332	3.019	−3.390	3.509	−3.065

Source(s): Authors' own work

Table 4. $i_{\text{abc-error+}}$和$i_{\text{abc-error-}}$ when a single tube fault

Fault type	$i_{\text{a-error+}}$	$i_{\text{a-error−}}$	$i_{\text{b-error+}}$	$i_{\text{b-error−}}$	$i_{\text{c-error+}}$	$i_{\text{c-error−}}$
T_1	3.224	0.03	−0.335	−1.319	−0.2387	−1.369
T_2	0.057	−3.408	1.287	0.385	1.305	0.192

Source(s): Authors' own work

(2) double tubes fault(same phase)

Taking the T_1 and T_2 faults as an example, Figure 21 shows the $i_{\text{abc-digital}}$ and $i_{\text{abc-error}}$ during the T_1 and T_2 faults. Table 5 presents the $i_{\text{abc-digital+}}$ and $i_{\text{abc-digital−}}$ during the T_1 and T_2 faults; Table 6 shows the $i_{\text{abc-error+}}$ and $i_{\text{abc-error−}}$ during the T_1 and T_2 faults. According to Tables 5 and 6, when T_1 and T_2 fail, $i_{\text{a-digital+}}$ is almost equal to $i_{\text{a-error+}}$, and $i_{\text{a-digital−}}$ is almost equal to $i_{\text{a-error-}}$, while the rest show significant deviations; the fault patterns for T_3, T_4 and T_5, T_6 are the same as those for T_1 and T_2. Therefore, the fault of double tubes on the same phase can be accurately diagnosed.

(3) double tubes fault(different phase and side)

Taking the T_1 and T_4 faults as an example, Figure 22 shows the $i_{\text{abc-digital}}$ and $i_{\text{abc-error}}$ during the T_1 and T_4 faults. Table 7 presents the $i_{\text{abc-digital+}}$ and $i_{\text{abc-digital−}}$ during the T_1 and T_2 faults; Table 8 shows the $i_{\text{abc-error+}}$ and $i_{\text{abc-error−}}$ during the T_1 and T_2 faults. According to Tables 7 and 8, when

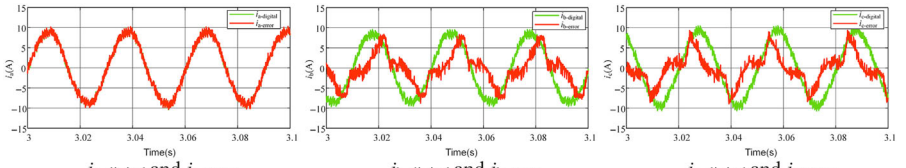

$i_{\text{a-digital}}$ and $i_{\text{a-error}}$ **(a)** $i_{\text{b-digital}}$ and $i_{\text{b-error}}$ **(b)** $i_{\text{c-digital}}$ and $i_{\text{c-error}}$ **(c)**

Figure 21. $i_{\text{abc-digital}}$ and $i_{\text{abc-error}}$ when T_1 and T_2 fault. Source: Authors' own work

Table 5. $i_{\text{abc-digital+}}$和$i_{\text{abc-digital-}}$ when T_1 and T_2 fault

Fault type	$i_{\text{a-digital+}}$	$i_{\text{a-digital−}}$	$i_{\text{b-digital+}}$	$i_{\text{b-digital−}}$	$i_{\text{c-digital+}}$	$i_{\text{c-digital−}}$
T_1, T_2	5.733	−5.763	5.624	−5.641	5.778	−5.879

Source(s): Authors' own work

Table 6. $i_{\text{abc-error+}}$和$i_{\text{abc-error-}}$ when T_1 and T_2 fault

Fault type	$i_{\text{a-error+}}$	$i_{\text{a-error−}}$	$i_{\text{b-error+}}$	$i_{\text{b-error−}}$	$i_{\text{c-error+}}$	$i_{\text{c-error−}}$
T_1, T_2	5.763	−5.786	2.259	−2.279	2.082	−2.114

Source(s): Authors' own work

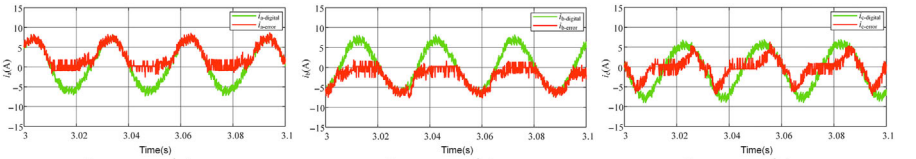

$i_{a\text{-digital}}$ and $i_{a\text{-error}}$ (a) $i_{b\text{-digital}}$ and $i_{b\text{-error}}$ (b) $i_{c\text{-digital}}$ and $i_{c\text{-error}}$ (c)

Figure 22. $i_{abc\text{-digital}}$ and $i_{abc\text{-error}}$ when T_1 and T_4 fault. Source: Authors' own work

Table 7. $i_{abc\text{-digital}+}$和$i_{abc\text{-digital-}}$ when T_1 and T_4 fault

Fault type	$i_{a\text{-digital}+}$	$i_{a\text{-digital}-}$	$i_{b\text{-digital}+}$	$i_{b\text{-digital}-}$	$i_{c\text{-digital}+}$	$i_{c\text{-digital}-}$
T_1, T_4	4.688	−4.061	4.427	−4.094	3.677	−4.720

Source(s): Authors' own work

Table 8. $i_{abc\text{-error}+}$和$i_{abc\text{-error-}}$ when T_1 and T_4 fault

Fault type	$i_{a\text{-error}+}$	$i_{a\text{-error}-}$	$i_{b\text{-error}+}$	$i_{b\text{-error}-}$	$i_{c\text{-error}+}$	$i_{c\text{-error}-}$
T_1, T_4	4.783	0.3457	−0.421	−4.468	1.298	−1.805

Source(s): Authors' own work

T_1 and T_4 fail, $i_{a\text{-digital}+}$ is almost equal to $i_{a\text{-error}+}$, and $i_{a\text{-digital}-}$ is almost equal to $i_{a\text{-error}-}$, while the rest show significant deviations; the fault patterns are the same as those for T_1 and T_4. Therefore, the fault of double tubes on the different sides and phases can be accurately diagnosed.

(4) double tubes fault(different phase and same side)

Taking the T_1 and T_3 faults as an example, Figure 23 shows the $i_{abc\text{-digital}}$ and $i_{abc\text{-error}}$ during the T_1 and T_3 faults. Table 9 presents the $i_{abc\text{-digital}+}$ and $i_{abc\text{-digital}-}$ during the T_1 and T_3 faults;

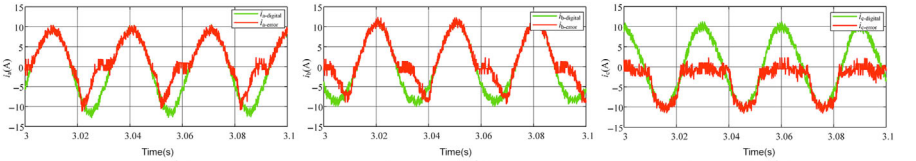

$i_{a\text{-digital}}$ and $i_{a\text{-error}}$ (a) $i_{b\text{-digital}}$ and $i_{b\text{-error}}$ (b) $i_{c\text{-digital}}$ and $i_{c\text{-error}}$ (c)

Figure 23. $i_{abc\text{-digital}}$ and $i_{abc\text{-error}}$ when T_1 and T_3 fault. Source: Authors' own work

Table 9. $i_{abc\text{-digital}+}$和$i_{abc\text{-digital-}}$ when T_1 and T_3 fault

Fault type	$i_{a\text{-digital}+}$	$i_{a\text{-digital}-}$	$i_{b\text{-digital}+}$	$i_{b\text{-digital}-}$	$i_{c\text{-digital}+}$	$i_{c\text{-digital}-}$
T_1, T_3	5.937	−7.17	6.982	−5.925	6.498	−6.466

Source(s): Authors' own work

Table 10 shows the $i_{abc\text{-}error+}$ and $i_{abc\text{-}error-}$ during the T_1 and T_3 faults. According to Tables 9 and 10, when T_1 and T_3 fail, $i_{a\text{-}digital+}$ is almost equal to $i_{a\text{-}error+}$, and $i_{a\text{-}digital-}$ is almost equal to $i_{a\text{-}error-}$, $i_{a\text{-}digital+}$ is almost equal to $i_{a\text{-}error+}$, and $i_{a\text{-}digital-}$ is almost equal to $i_{a\text{-}error-}$, while the rest show significant deviations. The fault patterns are the same as those for T_1 and T_3. Therefore, the fault of double tubes on the same side and different phases can be accurately diagnosed.

4. Experimental verification

Based on the theoretical analysis and simulation demonstration from the previous text, the small-power experimental platform for driving a permanent magnet synchronous motor system with a three-phase two-level inverter was utilized to validate the digital twin model of the system. Furthermore, the Speed-goat real-time simulation platform was employed to conduct hardware-in-the-loop experimental validation of the inverter IGBT fault diagnosis method based on the digital twin model.

4.1 Small power experimental platform

The experimental setup for the three-phase permanent magnet synchronous motor (PMSM) drive system is illustrated in Figure 24. The system configuration comprises a three-phase two-level voltage source inverter (VSI) coupled with a PMSM. The DC bus is powered by a Chroma programmable DC power supply. The control algorithm is implemented through digital signal processing using a TMS320F28335 DSP from Texas Instruments. Current measurement is performed using LEM LA55-P Hall-effect current sensors, while rotor position and speed detection are achieved through an AD2S1210 resolver-to-digital converter (RDC) from Analog Devices. A magnetic powder brake system is integrated for dynamic load

Table 10. $i_{abc\text{-}error+}$和$i_{abc\text{-}error-}$ when T_1 and T_3 fault

Fault type	$i_{a\text{-}error+}$	$i_{a\text{-}error-}$	$i_{b\text{-}error+}$	$i_{b\text{-}error-}$	$i_{c\text{-}error+}$	$i_{c\text{-}error-}$
T_1, T_3	5.970	−3.087	7.021	−2.884	−0.656	−6.559

Source(s): Authors' own work

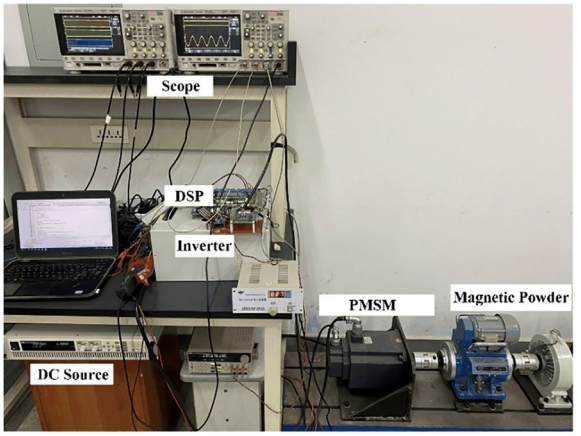

Figure 24. Three-phase permanent magnet synchronous motor drive system experimental platform. Source: Authors' own work

torque application. The detailed specifications of the PMSM under test are provided in Table 11.

4.2 Semi-physical experimental platform:
Figure 25 illustrates the hardware-in-the-loop (HIL) simulation platform for the three-phase PMSM drive system. The system architecture consists of a host computer running MATLAB/Simulink for mathematical modeling and simulation of the PMSM drive system. The compiled model is deployed to a Speedgoat real-time target machine for high-fidelity real-time simulation and data acquisition. The control algorithm is executed on a TMS320F28335 digital signal processor, which generates PWM signals for inverter switching control. The Speedgoat real-time system emulates the power circuit dynamics of the three-phase PMSM drive system, while simultaneously providing real-time physical data outputs for system verification and performance analysis.

4.3 Verification and analysis of the digital twin model for the PMSM drive system
4.3.1 Steady-state. Figure 26 shows the actual three-phase current and speed waveforms under steady-state conditions with the same speed and different load torques. Figure 26(a) has a load torque of 1N·m and a given speed of 500r/min. Figure 26(b) has a load torque of 9N·m and a given speed of 500r/min. Figure 27 shows the actual three-phase current and speed waveforms

Table 11. Permanent magnet synchronous motor parameters

Parameter	Value
DC voltage(U_{dc})	250V
Stator resistance(R_s)	0.71Ω
d-axis inductance(L_d)	6.24mH
q-axis inductance (L_q)	6.24mH
Permanent magnet flux linage(ψ_f)	0.421Wb
Pairs of poles(n_p)	4

Source(s): Authors' own work

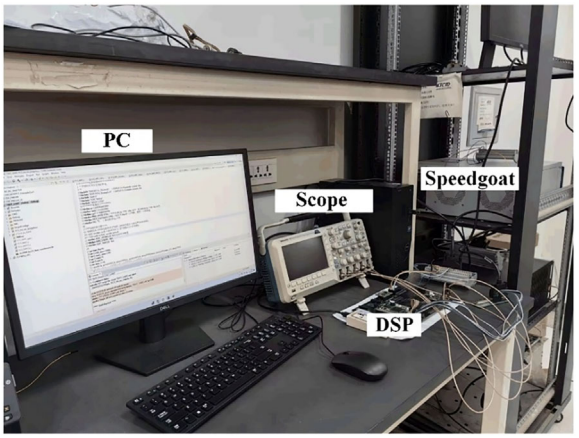

Figure 25. Semi-physical experiment platform. Source: Authors' own work

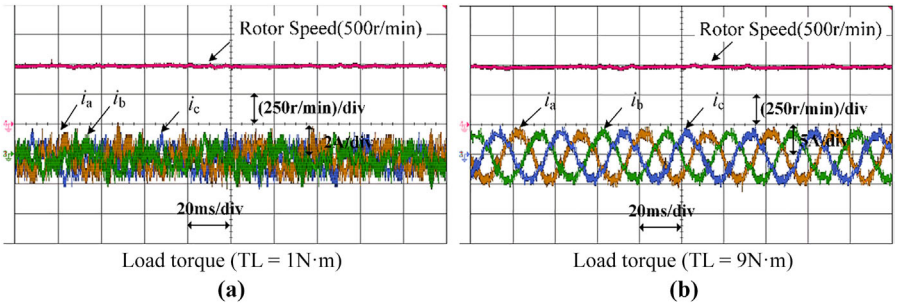

Figure 26. The three-phase current and speed waveforms under different loads. Source: Authors' own work

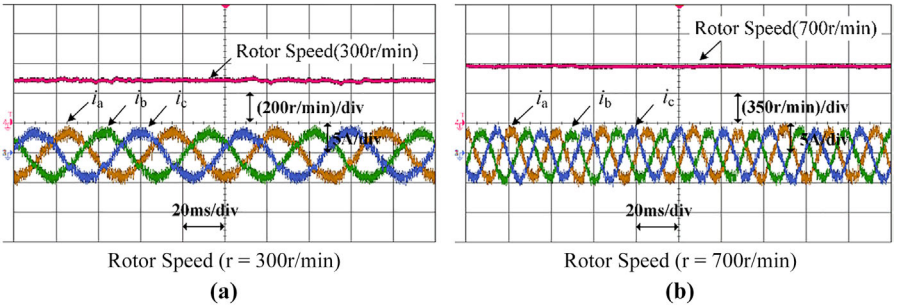

Figure 27. The three-phase current and speed waveforms under different speeds. Source: Authors' own work

under steady-state conditions with different speeds and the same load torque. Figure 27(a) has a load torque of 9N·m and a given speed of 300r/min, while Figure 27(b) has a load torque of 9N·m and a given speed of 700r/min. It can be seen that the speed reaches the given speed, and the three-phase current waveform is sinusoidal, indicating that the motor is operating normally.

Figures 28–31 provide a comparison of the three-phase current waveforms output by the digital twin model and the actual three-phase current waveforms under steady-state conditions. According to Figures 28 and 29, under the same speed and different load conditions, the phase current output by the digital twin model (Digital twin) is the same as the phase current output by the actual physical circuit (Physical data), meaning that the digital twin model has the same

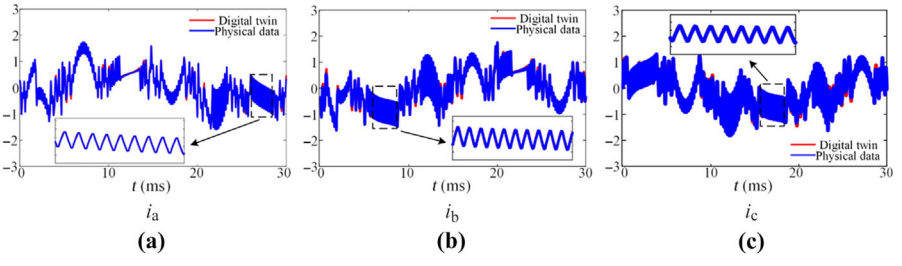

Figure 28. Comparison chart of digital twin and actual three-phase current waveforms (speed = 500 r/min, load torque = 1N·m). Source: Authors' own work

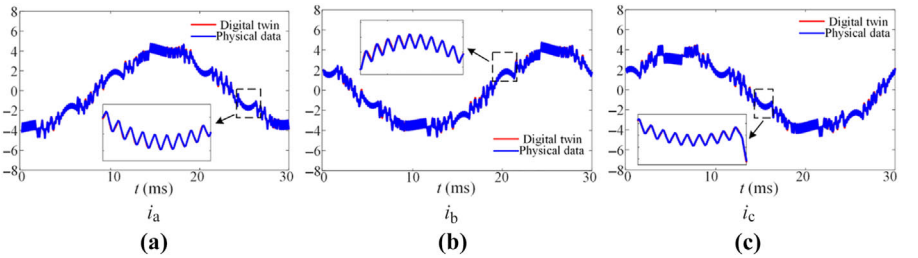

Figure 29. Comparison chart of digital twin and actual three-phase current waveforms (speed = 500 r/min, load torque = 9N·m). Source: Authors' own work

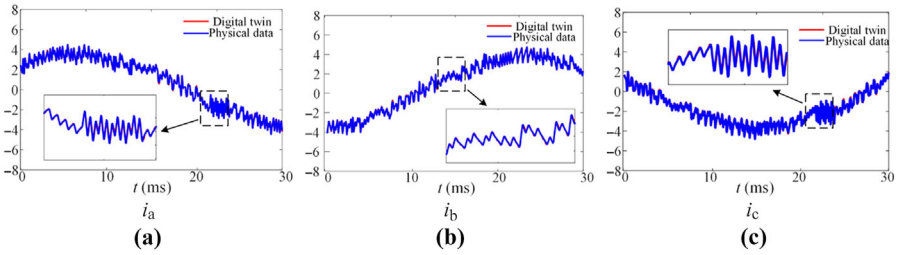

Figure 30. Comparison chart of digital twin and actual three-phase current waveforms (speed = 300 r/min, load torque = 9N·m). Source: Authors' own work

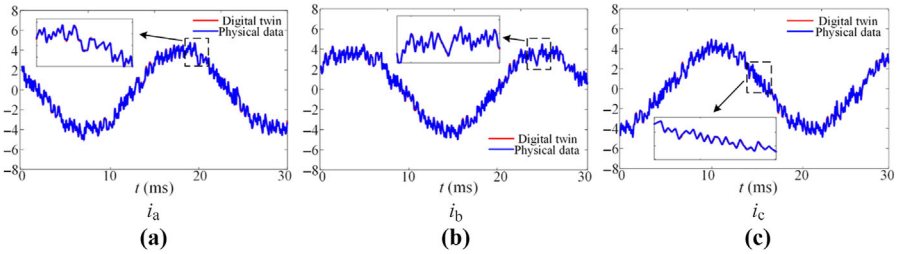

Figure 31. Comparison chart of digital twin and actual three-phase current waveforms (speed = 700 r/min, load torque = 9N·m). Source: Authors' own work

external characteristics as the actual physical prototype. According to Figures 29–31, under different speeds and the same load conditions, the phase current output by the digital twin model (Digital twin) is the same as the phase current output by the actual physical circuit (Physical data), indicating that the digital twin model possesses the same external characteristics as the actual physical prototype. Therefore, under steady-state conditions, the digital twin model of the three-phase permanent magnet synchronous motor drive system is sufficiently accurate in terms of external characteristics.

4.3.2 Dynamic. The operating conditions of the motor can change, which requires that the digital twin model must also maintain consistency with the actual physical circuit in dynamic situations. Figure 32 shows the actual three-phase current and speed waveforms under a load torque of 9N·m with varying speeds. Figure 32(a) simulates the motor acceleration condition, where the speed changes from 400r/min to 500r/min; Figure 32(b) simulates the motor

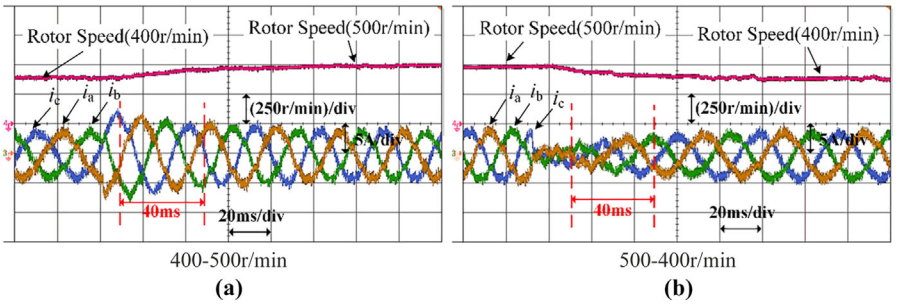

Figure 32. The three-phase current and speed waveforms under different speeds but the same load. Source: Authors' own work

deceleration condition, where the speed changes from 500r/min to 400r/min. Figure 33 shows the actual three-phase current and speed waveforms at a speed of 500r/min with varying load torques. Figure 33(a) simulates the motor loading condition, where the load torque changes from 1N·m to 9N·m; Figure 33(b) simulates the motor unloading condition, where the load torque changes from 9N·m to 1N·m.

Figures 34–37 show the comparison of the three-phase current waveforms output by the digital twin model and the actual three-phase current waveforms under dynamic conditions. According to Figures 34 and 35, under conditions of varying speed and the same load, the phase current output by the digital twin model (Digital twin) is the same as the phase current

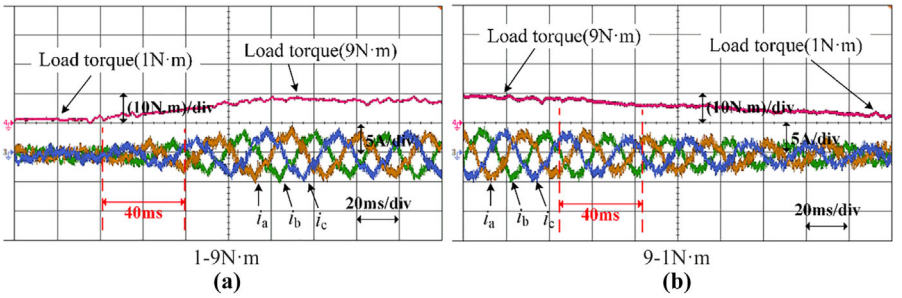

Figure 33. The three-phase current and speed waveforms under the same speed but different loads. Source: Authors' own work

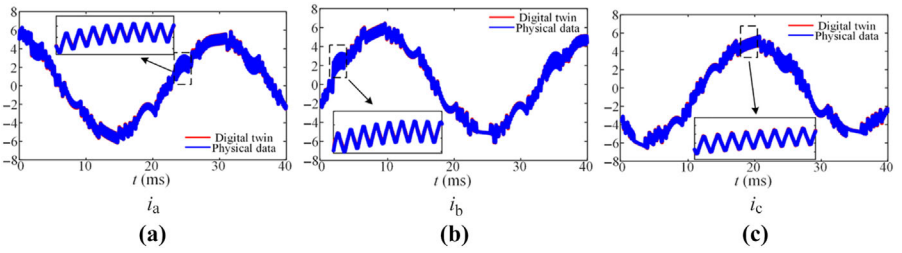

Figure 34. Comparison chart of digital twin and actual three-phase current waveforms (speed = 400-500r/min, load torque = 9N·m). Source: Authors' own work

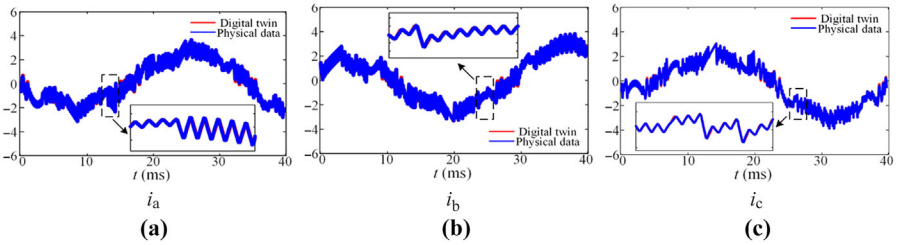

Figure 35. Comparison chart of digital twin and actual three-phase current waveforms (speed = 500-400r/min, load torque = 9N·m). Source: Authors' own work

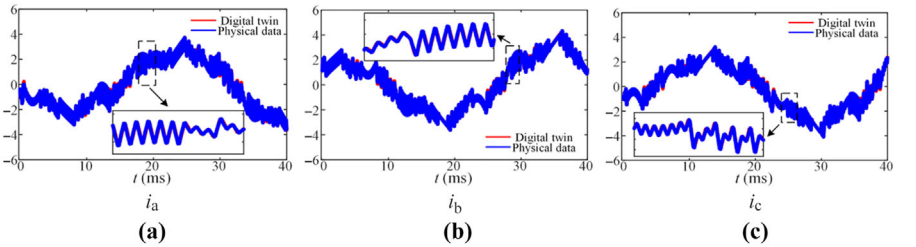

Figure 36. Comparison chart of digital twin and actual three-phase current waveforms (speed = 500r/min, load torque = 1-9N·m). Source: Authors' own work

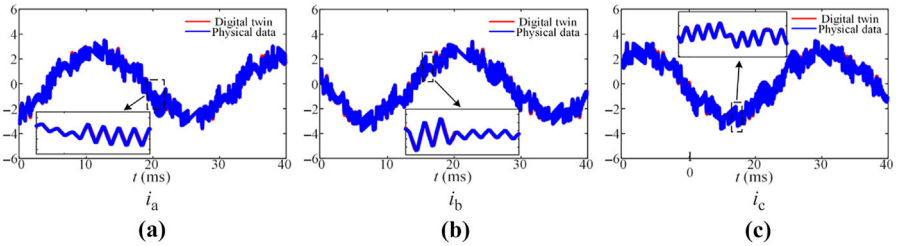

Figure 37. Comparison chart of digital twin and actual three-phase current waveforms (speed = 500r/min, load torque = 9-1N·m). Source: Authors' own work

output by the actual physical circuit (Physical data), meaning that the digital twin model possesses the same external characteristics as the actual physical prototype. According to Figures 36 and 37, under conditions of the same speed and varying load torque, the phase current output by the digital twin model (Digital twin) is the same as the phase current output by the actual physical circuit (Physical data), indicating that the digital twin model has the same external characteristics as the actual physical prototype. Therefore, under dynamic conditions, the digital twin model of the three-phase permanent magnet synchronous motor drive system is sufficiently accurate in terms of external characteristics.

4.4 Fault verification:

4.4.1 Single tube fault:. Figure 38 shows the $i_{abc\text{-}digital}$ and $i_{abc\text{-}error}$ during the T_1 fault. Within T_{a+}, $i_{a\text{-}digital}$ is consistent with $i_{a\text{-}error}$; within $T_{a\text{-}}$, $i_{a\text{-}digital}$ is not the same as $i_{a\text{-}error}$. Within T_{b+}, $i_{b\text{-}digital}$ is not consistent with $i_{b\text{-}error}$; within $T_{b\text{-}}$, i_{b}_digital is not the same as $i_{b\text{-}error}$. Within T_{c+}, $i_{c\text{-}}$

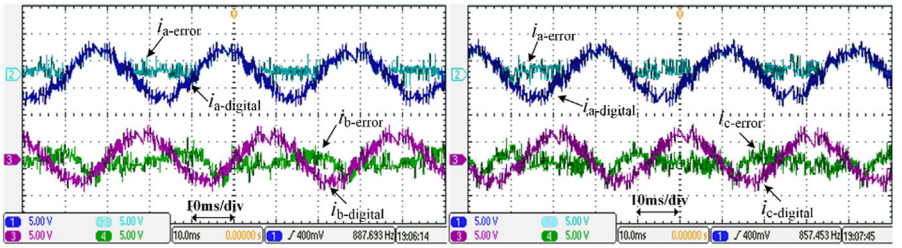

Figure 38. $i_{abc\text{-digital}}$ and $i_{abc\text{-error}}$ when T_1 is fault. Source: Authors' own work

$_{digital}$ is not consistent with $i_{c\text{-error}}$; within $T_{c\text{-}}$, $i_{c\text{-digital}}$ is not the same as $i_{c\text{-error}}$. According to Tables 12 and 13, during the T_1 fault, $i_{a\text{-digital}+}$ is almost equal to $i_{a\text{-error}+}$, while the others show significant deviations; during the T_2 fault, $i_{a\text{-digital}-}$ is almost equal to $i_{a\text{-error}-}$, while the others have significant deviations; the fault patterns for T_3, T_4, T_5, and T_6 are the same as those for the single tube T_1 and T_2. Therefore, consistent with the simulation analysis, single-tube open-circuit faults can be accurately diagnosed.

4.4.2 Double tube fault:.

(1) Coincident double tube fault:

Figure 39 shows the $i_{abc\text{-digital}}$ and $i_{abc\text{-error}}$ during the T_1 and T_2 faults. Within T_{a+}, $i_{a\text{-digital}}$ is consistent with $i_{a\text{-error}}$; within $T_{a\text{-}}$, $i_{a\text{-digital}}$ is consistent with $i_{a\text{-error}}$. Within T_{b+}, i_{b}_digital is not consistent with $i_{b\text{-error}}$; within $T_{b\text{-}}$, $i_{b\text{-digital}}$ is not the same as $i_{b\text{-error}}$. Within T_{c+}, $i_{c\text{-digital}}$ is not consistent with $i_{c\text{-error}}$; within $T_{c\text{-}}$, $i_{c\text{-digital}}$ is not the same as $i_{c\text{-error}}$. Table 14 shows the $i_{abc\text{-digital}+}$ and $i_{abc\text{-digital}-}$ during the T_1 and T_2 open-circuit faults; Table 15 shows the $i_{abc\text{-error}+}$ and $i_{abc\text{-error}-}$ during the T_1 and T_2 open-circuit faults. According to Tables 14 and 15, during the T1 and T2 faults, ia-digital+ is almost equal to $i_{a\text{-error}+}$, and $i_{a\text{-digital}-}$ is almost equal to $i_{a\text{-error}-}$, while the others show significant deviations; the fault patterns for T3, T4 are the same as those for T5, T6, which are similar to T1, T2. Therefore, consistent with the simulation analysis, the

Table 12. $i_{abc\text{-digital}+}$ and $i_{abc\text{-digital}-}$ when single tube fault

Fault type	$i_{a\text{-digital}+}$	$i_{a\text{-digital}-}$	$i_{b\text{-digital}+}$	$i_{b\text{-digital}-}$	$i_{c\text{-digital}+}$	$i_{c\text{-digital}-}$
T_1	2.647	−2.786	2.899	−2.851	2.799	−2.716
T_2	3.162	−2.988	3.058	−2.987	2.908	−2.846

Source(s): Authors' own work

Table 13. $i_{abc\text{-error}+}$ and $i_{abc\text{-error}-}$ when single tube fault

Fault type	$i_{a\text{-error}+}$	$i_{a\text{-error}-}$	$i_{b\text{-error}+}$	$i_{b\text{-error}-}$	$i_{c\text{-error}+}$	$i_{c\text{-error}-}$
T_1	2.709	0.776	−0.915	−0.834	−1.122	−0.654
T_2	−0.327	−3.031	1.023	0.809	0.922	1.059

Source(s): Authors' own work

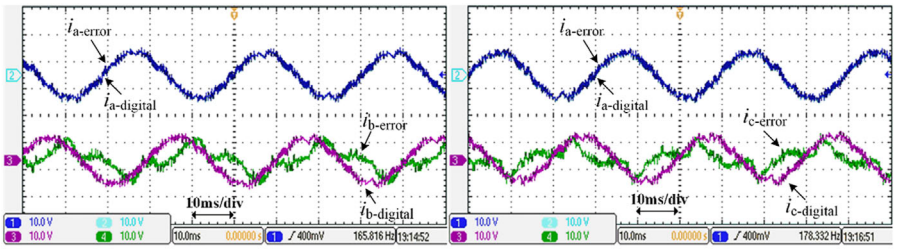

Figure 39. $i_{abc\text{-digital}}$ and $i_{abc\text{-error}}$ when T_1 and T_2 fault. Source: Authors' own work

Table 14. $i_{abc\text{-digital}+}$和$i_{abc\text{-digital}-}$ when T_1 and T_2 fault

故障类型	$i_{a\text{-digital}+}$	$i_{a\text{-digital}-}$	$i_{b\text{-digital}+}$	$i_{b\text{-digital}-}$	$i_{c\text{-digital}+}$	$i_{c\text{-digital}-}$
T_1, T_2	−5.605	5.681	5.611	−5.678	5.616	−5.693

Source(s): Authors' own work

Table 15. $i_{abc\text{-error}+}$和$i_{abc\text{-error}-}$ when T_1 and T_2 fault

故障类型	$i_{a\text{-error}+}$	$i_{a\text{-error}-}$	$i_{b\text{-error}+}$	$i_{b\text{-error}-}$	$i_{c\text{-error}+}$	$i_{c\text{-error}-}$
T_1, T_2	−5.597	5.694	2.073	−2.066	1.323	−1.392

Source(s): Authors' own work

open-circuit fault of the double tubes on the same phase and same side can be accurately diagnosed.

(2) Asynchronous and opposite-side double tube fault:

Taking the fault of T_1 and T_4 as an example, Figure 40 shows the $i_{abc\text{-digital}}$ and $i_{abc\text{-error}}$ during the fault of T_1 and T_4. Within the T_{a+} period, $i_{a\text{-digital}}$ is consistent with $i_{a\text{-error}}$; within the T_{a-} period, $i_{a\text{-digital}}$ is not consistent with $i_{a\text{-error}}$. Within the T_{b+} period, $i_{b\text{-digital}}$ is not consistent

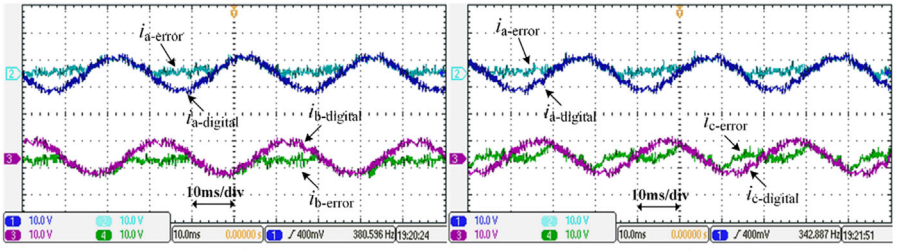

Figure 40. $i_{abc\text{-digital}}$ and $i_{abc\text{-error}}$ when T_1 and T_4 fault. Source: Authors' own work

with $i_{b\text{-}error}$; within the T_{b-} period, $i_{b\text{-}digital}$ is the same as $i_{b\text{-}error}$. Within the T_{c+} period, $i_{c\text{-}digital}$ is not consistent with $i_{c\text{-}error}$; within the T_{c-} period, $i_{c\text{-}digital}$ is not the same as $i_{c\text{-}error}$. Table 16 shows the $i_{abc\text{-}digital+}$ and $i_{abc\text{-}digital-}$ during the fault of T_1 and T_4; Table 17 shows the $i_{abc\text{-}error+}$ and $i_{abc\text{-}error-}$ during the fault of T_1 and T_4. According to Tables 16 and 17, when T_1 and T_4 fail, $i_{a\text{-}digital+}$ is almost equal to $i_{a\text{-}error+}$, and $i_{b\text{-}digital-}$ is almost equal to $i_{b\text{-}error-}$, while the rest have significant deviations; the patterns for other phase-disparate and side-disparate double tube failures (T_1, T_6; T_3, T_6; T_2, T_3; T_2, T_5; T_4, T_5) are the same as T_1, T_4. Therefore, consistent with the simulation analysis, phase-disparate and side-disparate double tube open-circuit faults can be accurately diagnosed.

(3) Asynchronous and same-side double tube fault:

Taking the fault of T_1 and T_3 as an example, Figure 41 shows the $i_{abc\text{-}digital}$ and $i_{abc\text{-}error}$ during the fault of T_1 and T_3. Within the T_{a+} period, $i_{a\text{-}digital}$ is consistent with $i_{a\text{-}error}$; within the T_{a-} period, $i_{a\text{-}digital}$ is not consistent with $i_{a\text{-}error}$. Within the T_{b+} period, $i_{b\text{-}digital}$ is consistent with $i_{b\text{-}error}$; within the T_{b-} period, $i_{b\text{-}digital}$ is different from $i_{b\text{-}error}$. Table 18 shows the $i_{abc\text{-}digital+}$ and $i_{abc\text{-}digital-}$ during the fault of T_1 and T_3; Table 19 shows the $i_{abc\text{-}error+}$ and $i_{abc\text{-}error-}$ during the fault of T_1 and T_3. According to Tables 18 and 19, $i_{a\text{-}digital+}$ is almost equal to $i_{a\text{-}error+}$, $i_{b\text{-}digital+}$ is almost equal to $i_{b\text{-}error+}$, and $i_{c\text{-}digital-}$ is almost equal to $i_{c\text{-}error-}$, while the rest have significant deviations. In this case, an open-circuit fault of T_1 and T_3 will cause T_6 to also exhibit fault characteristics, which may lead to the diagnosis of a three-tube fault. However, in

Table 16. $i_{abc\text{-}digital+}$和$i_{abc\text{-}digital-}$ when T_1 and T_4 fault

Fault type	$i_{a\text{-}digital+}$	$i_{a\text{-}digital-}$	$i_{b\text{-}digital+}$	$i_{b\text{-}digital-}$	$i_{c\text{-}digital+}$	$i_{c\text{-}digital-}$
T_1, T_4	4.108	−4.132	4.088	−4.149	4.155	−4.041

Source(s): Authors' own work

Table 17. $i_{abc\text{-}error+}$和$i_{abc\text{-}error-}$ when T_1 and T_4 fault

Fault type	$i_{a\text{-}error+}$	$i_{a\text{-}error-}$	$i_{b\text{-}error+}$	$i_{b\text{-}error-}$	$i_{c\text{-}error+}$	$i_{c\text{-}error-}$
T_1, T_4	4.306	1.012	−0.968	−4.378	1.303	−1.175

Source(s): Authors' own work

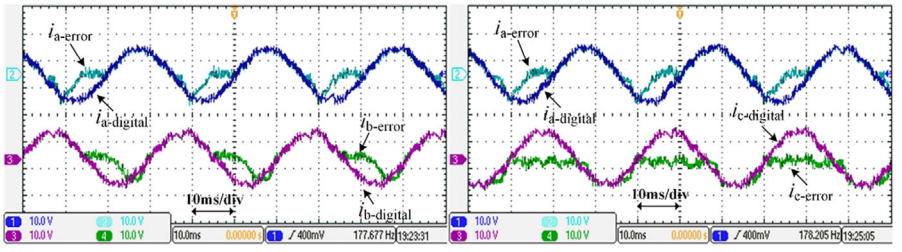

$i_{a\text{-}digital}$, $i_{a\text{-}error}$ and $i_{b\text{-}digital}$, $i_{b\text{-}error}$ (a)

$i_{a\text{-}digital}$, $i_{a\text{-}error}$ and $i_{c\text{-}digital}$, $i_{c\text{-}error}$ (b)

Figure 41. $i_{abc\text{-}digital}$ and $i_{abc\text{-}error}$ when T_1 and T_3 fault. Source: Authors' own work

Table 18. $i_{\text{abc-digital+}}$和$i_{\text{abc-digital-}}$ when T_1 and T_3 fault

Fault type	$i_{\text{a-digital+}}$	$i_{\text{a-digital-}}$	$i_{\text{b-digital+}}$	$i_{\text{b-digital-}}$	$i_{\text{c-digital+}}$	$i_{\text{c-digital-}}$
T_1, T_3	6.384	−6.289	6.279	−6.529	6.493	−6.404

Source(s): Authors' own work

Table 19. $i_{\text{abc-error+}}$和$i_{\text{abc-error-}}$ when T_1 and T_3 fault

Fault type	$i_{\text{a-error+}}$	$i_{\text{a-error-}}$	$i_{\text{b-error+}}$	$i_{\text{b-error-}}$	$i_{\text{c-error+}}$	$i_{\text{c-error-}}$
T_1, T_3	6.425	−2.224	6.312	−2.790	−1.245	−6.227

Source(s): Authors' own work

reality, a three-tube fault is almost impossible to occur. Therefore, when a three-tube fault is diagnosed, the fault is actually a phase-same side double tube fault, and the switch tube that is on a different side from the other two tubes is the one misdiagnosed (both T_1 and T_3 are on the upper bridge arm, belonging to the upper side; T_6 is on the lower bridge arm, belonging to the lower side). The patterns for other phase-same side double tube faults (T_1, T_5; T_3, T_5; T_2, T_4; T_2, T_6; T_4, T_6) are the same as T_1, T_3.

5. Conclusion

Aiming at the open-circuit fault problem of inverter IGBTs, this study proposes a digital twin model-based open-circuit fault diagnosis method. Taking the permanent magnet synchronous motor and its drive system as the research object, the phase current characteristics under different IGBT open-circuit fault types are analyzed. Firstly, the phase current characteristics under various fault modes are systematically elaborated. Secondly, a fault-free digital twin model of the permanent magnet synchronous motor and its drive system is constructed. By comparing the actual fault current with the current from the fault-free digital twin model, a fault diagnosis method based on current difference comparison is designed. This method calculates the average current value within the positive and negative half cycles of the current, and precisely locates the faulty IGBT position using the average current characteristics of the positive and negative half cycles. Simulation and experimental results demonstrate that the proposed digital twin model-based open-circuit fault diagnosis method can accurately diagnose and locate faulty IGBTs, providing a new solution for inverter fault diagnosis.

References

Choo, K. M., & Won, C. Y. (2020). Design and analysis of electrical braking torque limit trajectory for regenerative braking in electric vehicles with PMSM drive systems. *IEEE Transactions on Power Electronics*, *35*(12), 13308–13321. doi: 10.1109/tpel.2020.2994615.

Da, Y., Shi, X., & Krishnamurthy, M. (2012). A new approach to fault diagnostics for permanent magnet synchronous machines using electromagnetic signature analysis. *IEEE Transactions on Power Electronics*, *28*(8), 4104–4112. doi: 10.1109/tpel.2012.2227808.

Faiz, J., & Mazaheri-Tehrani, E. (2016). Demagnetization modeling and fault diagnosing techniques in permanent magnet machines under stationary and nonstationary conditions: An overview. *IEEE Transactions on Industry Applications*, *53*(3), 2772–2785. doi: 10.1109/tia.2016.2608950.

Glaessgen, E., & Stargel, D. (2012). The digital twin paradigm for future NASA and US Air Force vehicles. In *53rd AIAA/ASME/ASCE/AHS/ASC Structures, Structural Dynamics and Materials Conference 20th AIAA/ASME/AHS Adaptive Structures Conference 14th AIAA* (p. 1818).

Grieves, M. W. (2005). Product lifecycle management: The new paradigm for enterprises. *International Journal of Product Development*, *2*(1-2), 71–84. doi: 10.1504/ijpd.2005.006669.

Hammoud, I., Hentzelt, S., Xu, K., Oehlschlagel, T., Abdelrahem, M., Hackl, C., & Kennel, R. (2022). On continuous-set model predictive control of permanent magnet synchronous machines. *IEEE Transactions on Power Electronics*, *37*(9), 10360–10371. doi: 10.1109/tpel.2022.3164968.

Lin, S., Fang, X., Wang, X., Yang, Z., & Lin, F. (2021). Multiobjective model predictive current control method of permanent magnet synchronous traction motors with multiple current bounds in railway application. *IEEE Transactions on Industrial Electronics*, *69*(12), 12348–12357. doi: 10.1109/tie.2021.3128893.

Liu, K., Zhang, Q., Chen, J., Zhu, Z. Q., & Zhang, J. (2010). Online multiparameter estimation of nonsalient-pole PM synchronous machines with temperature variation tracking. *IEEE Transactions on Industrial Electronics*, *58*(5), 1776–1788. doi: 10.1109/tie.2010.2054055.

Liu, K., Zhu, Z. Q., & Stone, D. A. (2013). Parameter estimation for condition monitoring of PMSM stator winding and rotor permanent magnets. *IEEE Transactions on Industrial Electronics*, *60*(12), 5902–5913. doi: 10.1109/tie.2013.2238874.

Odhano, S. A., Bojoi, R., Roşu, Ş. G., & Tenconi, A. (2015). Identification of the magnetic model of permanent-magnet synchronous machines using DC-biased low-frequency AC signal injection. *IEEE Transactions on Industry Applications*, *51*(4), 3208–3215. doi: 10.1109/tia.2015.2413383.

Shi, Y., Sun, K., Huang, L., & Li, Y. (2011). Online identification of permanent magnet flux based on extended Kalman filter for IPMSM drive with position sensorless control. *IEEE Transactions on Industrial Electronics*, *59*(11), 4169–4178. doi: 10.1109/tie.2011.2168792.

Underwood, S. J., & Husain, I. (2009). Online parameter estimation and adaptive control of permanent-magnet synchronous machines. *IEEE Transactions on Industrial Electronics*, *57*(7), 2435–2443. doi: 10.1109/tie.2009.2036029.

Wang, Q., Zhang, G., Wang, G., & Xu, D. (2019). Offline parameter self-learning method for general-purpose PMSM drives with estimation error compensation. *IEEE Transactions on Power Electronics*, *34*(11), 11103–11115. doi: 10.1109/tpel.2019.2900559.

Wu, X., Fu, X., Lin, M., & Jia, L. (2019). Offline inductance identification of IPMSM with sequence-pulse injection. *IEEE Transactions on Industrial Informatics*, *15*(11), 6127–6135. doi: 10.1109/tii.2019.2932796.

Yang, S., Bryant, A., Mawby, P., Dawei Xiang, , Li Ran, & Tavner, P. (2011). An industry-based survey of reliability in power electronic converters. *IEEE Transactions on Industry Applications*, *47*(3), 1441–1451. doi: 10.1109/tia.2011.2124436.

Zhang, X., Liu, L., Wan, X., & Feng, B. (2021). Tool wear online monitoring method based on DT and SSAE-PHMM. *Journal of Computing and Information Science in Engineering*, *21*(3), 034501. doi: 10.1115/1.4050531.

Further reading

Miyashita, K., Yamashita, S., Tanabe, S., Shimozu, T., & Sento, H. (1980). Development of a high speed 2-pole permanent magnet synchronous motor. *IEEE Transactions on Power Apparatus and Systems*, *99*(6), 2175–2183. doi: 10.1109/tpas.1980.319780.

Odhano, S. A., Bojoi, R., Armando, E., Homrich, G., Filho, A. F. F., Popescu, M., & Dorrell, D. G. (2016). Identification of three-phase IPM machine parameters using torque tests. *IEEE Transactions on Industry Applications*, *53*(3), 1883–1891. doi: 10.1109/tia.2016.2646345.

Pellegrino, G., Vagati, A., Guglielmi, P., & Boazzo, B. (2011). Performance comparison between surface-mounted and interior PM motor drives for electric vehicle application. *IEEE Transactions on Industrial Electronics*, *59*(2), 803–811. doi: 10.1109/tie.2011.2151825.

Corresponding author
Kan Liu can be contacted at: bjliukan@163.com

Kan Liu received his B. Sc. degree in electrical engineering from Xi'an Jiaotong University in 2015, and the M. Sc. degree in electrical engineering from the University of Melbourne in 2018. He is currently a Research Assistant in the AC Transmission Development Department at Beijing Zongheng Electro-Mechanical Technology Co., Ltd. His current research interests include sensorless rail transit traction control, and advanced chopper control technologies, and their applications in modern traction drive systems.